Nanoscale

Accepted Manuscript

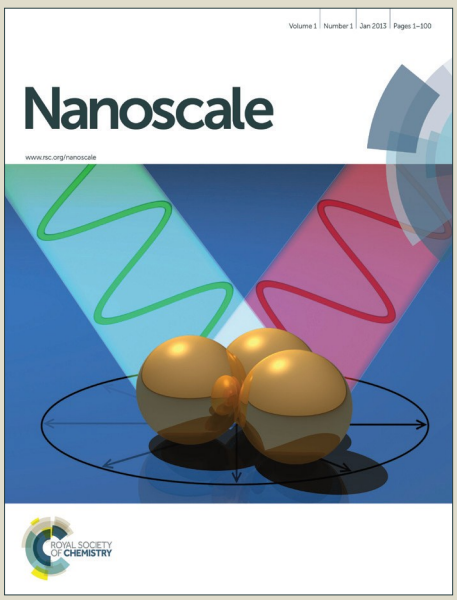

ROYAL SOCIETY OF CHEMISTRY

www.rsc.org/nanoscale

Iron Oxide Nanorods as High–Performance Magnetic Resonance Imaging Contrast Agents

Jeotikanta Mohapatra[1] Arijit Mitra[2] Himanshu Tyagi[2] D. Bahadur[1, 3, *] M. Aslam[1, 2, *, ╫]

[1] Centre for Research in Nanotechnology and Science (CRNTS), [2] Department of Physics, [3] Department of Metallurgical Engineering and Materials Science, Indian Institute of Technology Bombay, Powai, Mumbai-400076, India

**To whom correspondence should be addressed. E-mail: m.aslam@iitb.ac.in (M. Aslam). Phone: +91 22 2576 7585, dhirenb@iitb.ac.in (D. Bahadur), +91-22-2576 7632*

╫*Visiting scholar, Materials Science and Engineering Department, Northwestern Univeristy, Evanston, IL-60201*

Abstract

An efficient magnetic resonance imaging (MRI) contrast agent with high R_2 relaxivity value is achieved by controlling the shape of iron oxide to a rod like morphology with a length 30-70 nm and diameter 4-12 nm. Fe_3O_4 nanorods of length 70 nm, encapsulated with polyethyleneimine show very high R_2 relaxivity value of 608 $mM^{-1}s^{-1}$. The enhanced MRI contrast of nanorods is attributed to higher surface area and anisotropic morphology. The higher surface area induces a stronger magnetic field perturbation over a larger volume more effectively for the outer sphere protons. The shape anisotropy contribution is understood by calculating the local magnetic field of nanorod and spherical nanoparticle under an applied magnetic field (3 Tesla). As compared to spherical geometry, the induced magnetic field of rod is stronger and hence the stronger magnetic field over a large volume leads to higher R_2 relaxivity for nanorods.

Keywords: Magnetic nanorods, Superparamagnetism, Magnetic resonance imaging, Contrast agent

1. Introduction

Magnetic nanoparticles (MNPs) have been established for use in various promising biomedical applications, such as contrast agent in magnetic resonance imaging (MRI),[1-6] vector in drug delivery[7-9] and mediator to convert electromagnetic energy to heat.[9-11] The MNPs based MRI contrast agent, can improve diagnosis in several pathologies.[12,13] Iron oxide NPs (Fe_3O_4) of several formulations such as Resovist, Combidex and Feridex have been used as T_2 weighted contrast agent to accelerate R_2 relaxivity of protons.[13] However, these commercial contrast agents have relatively low R_2 relaxivity, as they are synthesized in aqueous medium and consequently have poor crystallinity, large size dispersion (standard deviation: $\sigma > 20$ %) and a compromised magnetic moment.[14] The R_2 relaxivity enhancement is mainly proportional to saturation magnetization (M_S) value and surface area of MNP. To achieve high-performance i.e. darker contrast or shorter T_2, several attempts have been made to improve the magnetic moment through control of the size, dopant and surface properties of MNPs.[3, 15-17] The size of iron oxide NPs is varied precisely (4-14 nm) by controlled crystallization through thermolysis of iron salt in organic surfactants. The magnetization of iron oxide NPs is also tailored by doping various transition metals such as Zn, Ni, Co, and Mn. Since both surface area and M_S increases with an increase of the NPs size, a linear relationship is observed between R_2 relaxivity vs. nanoparticle size.[3] For example, Cheon et. al. found that the R_2 value of the iron oxide NPs gradually increases from 78 $mM^{-1}s^{-1}$ to 106, 130 and to 218 $mM^{-1}s^{-1}$ as the NPs size increases from 4 nm to 6, 9 and 12 nm, respectively.[18] Despite all these improvements, it is further possible to optimize the magnetic properties, surface area and accordingly the R_2 relaxivity of Fe_3O_4 nanoparticles by controlling the shape. The shape anisotropy could induce very strong localized magnetic field inhomogeneity, as the induced magnetic field strength is also actively depends on shape of the MNP, due to the so-called demagnetization effect.[19] Although the anisotropic NPs have promising advantages over the spherical shape, but the use of NPs with anisotropic

configuration has not been well demonstrated in the literature because their preparation is a challenging task as the surface energy favors the formation of spherical nanoparticles.[20, 21]

Our group has been exploring new materials with enhanced MR contrast properties over the last few years.[22-26] To study the effect of shape on MRI contrast enhancement, we have synthesized spherical and faceted irregular (FI) $CoFe_2O_4$ nanostructures *via* a high temperature solution phase method.[22] Similar sized FI structures with lower M_S values than the spherical $CoFe_2O_4$ nanostructures show a higher R_2 value. The enhanced contrast properties is attributed to the differences in surface area between spherical and FI nanostructures, which is higher in case of FI nanostructures. Recently, Zhao et. al. demonstrated that octapod Fe_3O_4 NPs of edge length of 30 nm exhibit an ultra-high R_2 relaxivity value (679.3±30 mM^{-1} s^{-1}) as compared to spherical counterpart of similar material volume.[27] The high R_2 relaxivity of octapod shaped NPs is believed to be due to anisotropic shape, which renders a higher surface area than the similar material volume spherical shape. The increased surface area allows a greater number of hydrogen nuclei of water in proximity. Therefore, a greater number of neighboring nuclei are disturbed by the dipolar field of the NPs, resulting in faster relaxation. There are also few reports on MRI contrast characteristics of nanorods (NRs) of praramagnetic compounds such as $Dy(OH)_3$, $Gd(OH)_3$ and β-FeOOH.[28-30] Even though these paramagnetic compounds possess low magnetic moment (< 10 emu/g), due to higher surface area their R_2 relaxivity is found to be comparable to commercial Fe_3O_4 NPs contrast agents. Furthermore, as compared to spherical NPs, NRs offer longer blood circulation times, stronger interaction with tumors, enhanced retention at tumor sites and improved targeting efficiency, making them excellent candidates as targeting carriers or MRI contrast agents.[31] To the best our knowledge, there is no report on MR contrast properties of Fe_3O_4 NRs.

Herein, we demonstrate a simple two step reaction strategy for the synthesis of uniform 'colloidal' magnetite nanorods (30-70 nm in length) with very high R_2 relaxivity

values. We found that the relaxation coefficient (R_2) gradually increases from 312 to 608 $s^{-1}mM^{-1}$ with an increase in the length of NRs; this increase is a consequence of magnetization enhancement as well as sharp increase in the surface area due to anisotropic morphology. Although the spherical NPs exhibit high magnetization than the NRs of same material volume, but a high relaxivity is realized for NRs. The enhanced MR contrast characteristics for NRs correspond to the larger surface area rendered due to the anisotropic morphology.

2. Experimental section

a. Preparation of β-FeOOH nanorods

Rod-shaped FeOOH nanostructure was prepared by hydrolysis of $FeCl_3$ aqueous solution. In a typical synthesis of 70 nm length FeOOH NRs, 20 mmol of $FeCl_3 \cdot 6H_2O$ was added to a round-bottom flask containing 100 ml of deionized water with 0.2 ml polyethyleneimine (PEI). The reaction mixture was heated at 80 °C under magnetic stirring for 2 h to obtain uniform rod-shaped FeOOH nanostructure. The precipitate was separated by centrifugation and washed several times with deionized water and ethanol. The length of NRs is controlled from 25-70 nm by varying the PEI content as 2, 1.5, 1, 0.5, 0.3 and 0.2 ml. Further, a decrease of PEI content to 0.1 ml and below transformed the rod-shape morphology of FeOOH to a spindle shaped structure of length above 100 nm.

b. Preparation of Fe_3O_4 nanorods

Fe_3O_4 NRs were synthesized as follows: 500 mg of FeOOH nanorods and 25 mmol of oleylamine were taken in three necked round bottom flask. Under nitrogen ambience, the solution was heated to 200 °C for 4 h. The final product was subjected to magnetic separation and washed with a mixture of hexane and acetone for several times to remove any uncoordinated amine molecules. The detail of the synthesis approach is depicted in Scheme 1. The morphology of NRs was retained even after the reduction at 200 °C.

c. Preparation of Fe_3O_4 nanoparticles

Uniform Fe_3O_4 nanoparticles ($\sigma \leq 15\%$) are prepared using our previously published protocol.[32] In a typical synthesis of 6 nm Fe_3O_4 nanoparticles, a mixture of 5 mM of $FeCl_2$ and 25 mM of oleylamine (amine to precursor molar ratio 5:1) was heated at 200 ˚C under N_2 atmosphere. The size was controlled with the molar ratio of precursor to amine as 1:3 (9 nm) and 1:7 (4 nm), respectively. To further increase the particle size above 9 nm, a seed-mediated growth model was utilized.[33] For example, the smaller nanoparticles of 6 nm were first mixed (in different quantity of 100 mg or 150 mg) with more precursor materials and the mixture was heated as per the above procedure to achieve 12 nm and 16 nm Fe_3O_4 nanoparticles, respectively.

d. Surface functionalization towards 'colloidal' suspension

To use these samples as MRI contrast agent, as prepared Fe_3O_4 NRs were subjected to surface modification with polyethyleneimine (using ligand exchange approach as depicted in Fig. S1). 100 mg of the as prepared Fe_3O_4 NRs were dispersed in 10 mL of toluene and mixed with 10 ml of dimethylformamide (DMF) containing 2 ml of PEI. Under N_2 ambience, the mixture was then continuously stirred at 80 °C for 8 h. After the reaction, the final product was subjected to magnetic separation and was washed with ethanol several times to remove uncoordinated PEI molecules. The functionalized nanorods were dispersed in deionized water and taken for phantom MRI imaging. Similar to NRs, the aqueous suspension of the amine coated nanoparticles is also prepared through surface modification with polyethyleneimine (PEI).

e. Characterization Techniques

X-ray diffraction (XRD) spectra were retrieved from Xpert PANAlytic X-ray diffractometer with Cu Kα radiation (λ = 1.54 Å). FTIR spectra were taken on Bruker, Vertex-80 using KBr pellet. The XPS analysis was performed on a Thermo VG Scientific MultiLab, ESCA Probe using Mg Kα ($h\nu$ = 1253.6 eV) as the exciting source for

identification of the elements and their oxidation state. High-resolution transmission electron microscopy images and selected area diffraction patterns were obtained with JEOL JEM 2100F, field emission gun transmission electron microscope (FEG-TEM) at an accelerating voltage of 200 kV. The scanning electron micrographs (SEM) were taken by JSM-7600F FEG SEM. Thermogravimetric analysis (TGA) of coated Fe_3O_4 nanoparticles was carried out using a Perkin-Elmer Pyris instrument. TGA measurements were made from room temperature to 600 °C with a heating rate of 10 °C /min. The ζ-potential measurements were carried out by the Zetasizer nano series, Malvern Instruments. The magnetic properties of the samples were studied using physical property measurement system (Quantum Design PPMS). The isothermal magnetization (M) versus applied magnetic field (H), zero-field-cooled (ZFC), and field-cooled (FC) measurements were performed over the temperature range 10–300 K with applied field of 40 kOe. The applied external field for ZFC and FC isotherm was 200 Oe. To measure the T_2 relaxivity, PEI protected Fe_3O_4 nanorods with different Fe concentrations (0.005 -0.12) were diluted in DI water. The samples were scanned using a multi-echo T2-weighted fast spin echo imaging sequence (TR/TE=3500/30, 45, 60, 75, 90 and 105 ms, slice thickness = 2 mm) by a 3T Philips Achieva MR scanner.

3. Results and Discussion

Fig. 1a shows the X-ray diffraction pattern of 70 nm FeOOH NRs produced by hydrolysis of $FeCl_3$. All diffraction peaks of FeOOH are indexed to tetragonal phase of β-FeOOH (ICDD 34-1266). Reduction of the β-FeOOH NRs in oleylamine at 200 °C transforms the phase to magnetite (Fe_3O_4) (Scheme 1). The XRD pattern in Fig. 1b confirms the transformation of β-FeOOH to Fe_3O_4. The calculated lattice parameter of Fe_3O_4 NRs is 8.39 Å, which is in agreement with the reported value (ICDD 19-629). For further confirmation of the magnetite phase formation (and not the maghemite phase), X-ray photoelectron spectroscopy (XPS) spectrum is recorded after the reduction process (shown as Fig. 1c). The Fe_3O_4 nanorods show photoelectron peaks at 711.9 and 725.5 eV; the characteristic doublet ($Fe2p_{3/2}$ and

$Fe2p_{1/2}$) of iron oxide matches very well with the magnetite i.e. Fe_3O_4 phase as has been reported in literature.[34, 35] In case of FeOOH nanorods, this doublet appears at 711 and 724.2 eV, respectively. In addition, a small characteristic satellite peak of the Fe2p spectrum (octahedral Fe^{3+}) of β-FeOOH sample appears at 720 eV. After phase transformation, this particular peak position shifts to 716 eV, a characteristic of Fe^{2+} presence in octahedral site of magnetite phase.[34] This further confirms the phase conversion from β-FeOOH to Fe_3O_4.

. FeOOH NRs of different lengths and diameter are produced by using PEI as capping agent (Fig. S2, ESI). It is found that in the absence of PEI, the prepared sample possesses spindle shape morphology with larger length (150 nm) and diameter (35 nm). However, the addition of proper amount of PEI to the reaction mixture leads to formation of FeOOH NRs of thinner diameter. The average lengths of NRs obtained are 25, 30, 40, 50, 60 and 70 nm (Standard deviation, $\sigma \leq 20$ %) for 2 ml, 1.5 ml, 1 ml, 0.5 ml, 0.3 ml and 0.2 ml of PEI, respectively. The effect of PEI amount on shape, length and diameter of FeOOH particles is summarized in Table S1 (ESI). We found that by increasing the PEI concentration from 0.2 to 2 ml, the length and diameter of the FeOOH NRs can be controlled from 70 to 25 nm and 12 to 3 nm, respectively. This control over nanorods length and diameter with the PEI content is due to the adsorption of the protonized PEI on the lateral plane (200) of the nanorods.[36, 37] The NRs produced with 2 ml PEI content (25 nm in length) shows poor crystallinity (Fig. S3a-b, ESI). When FeOOH NRs is reduced to Fe_3O_4 phase by using oleylamine (which is multifunctional: acts as solvent, reducing and capping agent) at 200 °C, shape and size of the nanorods are retained (Fig. 2a-d). The transformation of the phase (FeOOH to Fe_3O_4) and retention of rod shape morphology could be due to the multifunctional properties (solvent, surfactant and reductant) of the oleylamine. In this case oleylamine act as an electron donor at elevated temperatures (200 ˚C) and leads to the formation of Fe_3O_4 nanorods.[38] However, the Fe_3O_4 sample produced from 25 nm length FeOOH NRs shows irregular shape and size (Fig. S3c-d, ESI). It could be due to amorphous

nature of the initial precursor material (as confirmed from the XRD data) and the reduction process occurs through dissolution and recrystallization of FeOOH NRs.[20] Selected area electron diffraction (SAED) measurements are taken to further confirm the crystalline phase of NRs. The SAED pattern of Fe_3O_4 NRs shows six prominent rings which could be indexed to reflections from five crystal planes of (220), (311), (400), (511) and (440).[32] This also supports the transformation of FeOOH to Fe_3O_4 phase.

Fig. 3a-e shows the transmission electron microscopy (TEM) images of spherical Fe_3O_4 nanoparticles of size 4, 6, 9, 12 and 16 nm (Standard deviation, $\sigma \leq 15$ %) prepared by thermolysis of $FeCl_2$ in the presences of oleylamine as multifunctional (solvent, reducing and surface functionalizing) agent. The TEM images confirm that the prepared nanoparticles are uniform in shape and size. The HRTEM image (Fig. 3f) confirms the crystallinity of the as synthesized nanoparticles with 0.251 nm d-spacing corresponding to [311] plane. Similar to NRs, the aqueous suspensions of the amine coated nanoparticles were also prepared through surface modification with polyethyleneimine (PEI).

To prepare stable colloidal suspension, as prepared Fe_3O_4 NRs are subjected to surface modification with polyethyleneimine (PEI). The surface PEI molecular coating is confirmed from the Fourier transform infrared (FTIR) spectroscopy, thermogravimetric analysis (TGA) and ζ-potential measurements. Fig. 4a shows a comparative analysis of FTIR spectra of PEI coated FeOOH (70 nm), oleylamine and PEI coated 70 nm Fe_3O_4 NRs. In FeOOH sample, the low frequency bands at 556, 614, 695 and 825 cm^{-1} were assigned to the Fe–O vibrational modes in β-FeOOH.[39] After reducing FeOOH at 200 °C in oleylamine, these bands disappear and a new peak appears at around 569 cm^{-1} which corresponds to Fe−O vibrational mode (Fe^{3+} bond) at octahedral and tetrahedral sites. The presence of Fe-O vibrational mode at 569 cm^{-1} could be attributed to magnetite phase of Fe_3O_4 since the Fe-O band for γ- Fe_2O_3 is usually seen at 540 cm^{-1}.[32] The strong IR peak in the range of 3745 cm^{-1} is assigned to N−H stretching mode of primary amine, while the C−N stretching, NH_2

scissoring and NH_2 wagging bands appears at 1074 cm^{-1}, 1447 cm^{-1} and 885 cm^{-1} respectively.[40] The bands at 2845 and 2920 cm^{-1} are assigned to vibrations from CH_2 groups in the long chain amine. In comparison with oleylamine−Fe_3O_4 NRs, PEI−Fe_3O_4 samples show strong IR peaks of C−N stretching, NH_2 scissoring and NH_2 wagging which corroborates the presence of PEI on the surface of Fe_3O_4 NRs. The thermogravimetric degradation profiles (Fig. S4, ESI) of the as-prepared and PEI-coated Fe_3O_4 NRs shows prominent weight loss of 9 % and 15 % over the temperature range of 150-450 °C, which could be attributed to the decomposition of the organic molecules attached to the NRs surface. The increase of 6% weight loss after the surface modification of NRs confirms the presence of PEI on the nanorod surface. Further, the positive zeta potential values in the pH range 2-11 (Fig. 4b) also supports the presence of the PEI amine groups at the NRs surface. The PEI modified Fe_3O_4 NRs are very stable as water colloids for about a month and no aggregation is observed (inset of Fig. 4b). There is no precipitation in water over a wide pH range (pH adjusted between 2– 9 by using HCl or NaOH). Moreover, TEM micrographs show no change in size and shape after the ligand exchange with PEI at a temperature of 80 °C (Fig. S5, ESI). The hydrodynamic diameters of the PEI functionalized Fe_3O_4 NRs are measured by dynamic light scattering (DLS: Fig S6a-c, ESI). The mean hydrodynamic diameters (Table S2, ESI) are larger than the size obtained from TEM, due to the presence of associated and hydrated long chain PEI layers.[41] Time dependent DLS study shows that the hydrodynamic size of the NRs does not change over a time frame of one week, indicating no aggregation of NRs.[42] Such stable PEI functionalized magnetite NRs suspension is highly desirable for a wide range of biomedical applications, as the PEI coating was found to enhance the nanoparticle uptake into cells and facilitates endosomal escape for the nucleotide delivery.[43] Further, PEI also has potential advantage in facilitating DNA and siRNA delivery.

Fig. 5a shows the temperature dependence of magnetization curve in the zero field cooled (ZFC) and field cooled (FC) protocols under an applied field of 200 Oe for the

Fe_3O_4 NRs of different sizes. The blocking temperatures (T_B) (i.e. the peak temperature of ZFC curve) for 30 nm and 40 nm Fe_3O_4 NRs are 80 K and 110 K, respectively. While for NRs of length above 40 nm, the blocking temperature is not observed and features of the curve are interestingly dominated by Verwey transition observed at 120 K.[44, 45] Verwey transition is a characteristic property of Fe_3O_4 and is seen in perfect stoichiometry. In case of smaller length NRs, the surface dead layer and surface oxidation makes the particles sufficiently non-stoichiometric and thus Verwey transition is not observed. Fig. 5b shows the ZFC and FC magnetization data of the spherical nanoparticles of different sizes. With an increase in nanoparticles size from 4 – 16 nm, T_B is observed to increase from 45 K to 240 K. The increase in T_B is attributed to an increase in anisotropic energy with an increase in volume which is consistent with the expression used to calculate the average blocking temperature $\langle T_B \rangle = K_{eff}V/25k_B$ (where k_B is the Boltzmann constant and K_{eff} is the anisotropy constant).[46] Room temperature hysteresis curves of the Fe_3O_4 NRs are shown as Fig. 5c. The coercivity and remanence values are not discernible at 300 K, indicating a superparamagnetic behavior of 30-70 nm length Fe_3O_4 NRs. The saturation magnetization (M_S, magnetization at 40 kOe) gradually increases from 50 emu/g to 66 emu/g with an increase in length of nanorod from 30 nm to 70 nm. The smaller magnetization values for nanorods as compared to bulk value (92 emu/g for magnetite[32]) are believed to be due to the existence of a surface spin disorder layer, which decreases with the increase of the particle diameter. Interestingly, in comparison to NRs, the M_S values of nanoparticles are higher (Fig. 5d). For example, the M_S value for 50 nm NRs is 58 emu/g, while that for same volume NPs (volume of 50 nm NR is nearly equal to that of 16 nm NPs, ESI, Table S4) is 83 emu/g. However, from M (T) curve we have seen Verwey transition (bulk phenomenon) in 50-70 nm length NRs, which suggests the absence of surface oxidized layer. Therefore, we believe the low magnetization might be due to the surface spin canting as well as shape anisotropy of the NRs, which prevent them from magnetizing in directions other than along their easy

magnetic axis.[47] For the random orientation of NRs, the projection of the magnetization vectors along the field direction will be smaller than that for a collection of nanoparticles without shape anisotropy effect.[48]

For *in vitro* applications, the cytocompatibility is investigated using Sulphorhodamine-B (SRB) assay to assess whether these magnetite NRs have any deleterious biological properties (Fig. S7, ESI). The SRB assay results indicate that the viability of the HeLa cells is not affected by the mere presence of NRs and the cells register normal growth, suggesting that particles are reasonably biocompatible and do not have toxic effect for *in vitro* use. The SRB assay shows that nearly 90 % of the cells are viable, even after incubation with 1 mg/ml of NRs.

The T_2 weighted MR images of PEI modified Fe_3O_4 NRs and NPs at different iron concentrations are recorded at 3T. The obtained phantom shows a significant signal attenuation with increasing concentration of Fe from 0.008 to 0.12 mmol (Fig. 6a and 6c). The corresponding relaxation rates ($R_2=1/T_2$) exhibit a linear trend with Fe concentration as shown in Fig. 6b and 6d. The R_2 values for Fe_3O_4 NRs with lengths of 30, 40, 50, 60 and 70 nm are 312, 381, 427, 545 and 608 $s^{-1}mM^{-1}$, respectively (Fig. 6b). The increasing trend of R_2 values with the length of nanorods is possibly due to the enhancement of magnetization value as well as surface area (responsible for the field perturbation areas for the outer sphere protons), which was found to increase with increase of the NRs length. Fig. 6d shows that R_2 relaxivity values of Fe_3O_4 NPs increase from 141 to 297 $s^{-1}mM^{-1}$ with increase in the size from 4 to 16 nm. From the magnetic data, it is observed that the NPs exhibit higher magnetization value as compared to NRs, while the observed R_2 is counter-intuitive and higher in case of lower susceptibility nanorods. For example, the M_S value of 16 nm Fe_3O_4 NPs is 83 emu/g and that for 50 nm NRs (equivalent material volume) is 58 emu/g. Although the M_S value of NRs is less than NPs by 25 emu/g but the NRs exhibits nearly 1.5 times higher R_2 value. Similarly, the 8 and 12 nm NPs have equivalent material volume to 30 and

40 nm length NRs, respectively. However, the R_2 values of NPs (8 nm; 218 $s^{-1}mM^{-1}$ and 12 nm; 249 $s^{-1}mM^{-1}$) are much lower than the NRs (30 nm; 312 $s^{-1}mM^{-1}$ and 40 nm; 381 $s^{-1}mM^{-1}$). The difference in R_2 values between NRs and NPs of equivalent material volume can be understood by considering the outer sphere theory, which comprises the diffusion and dephasing of protons around magnetic field inhomogeneity of a magnetic nanoparticle. According to Hwang and Freed's theory, the R_2 value is proportional to the square of M_s and the effective magnetic diameter (Equation S1, ESI note A).[27] In general, the M_s value determines the local magnetic field inhomogeneity and the effective diameter defines the field perturbation area for the outer sphere protons. The field perturbation area is directly related to surface area of nanostructures and in our case NRs possess higher surface area than NPs of similar solid volume (Table S3). For example, the surface area of NRs of length 50 nm is nearly 1.5 times higher than the surface area of NPs of size 16 nm which has the equivalent material volume. Therefore, the NRs are considered to be able to generate a larger area of local field inhomogeneity as compared to NPs under an applied magnetic field. The local magnetic field generated by 9-16 nm NPs and 30-70 nm length NRs are calculated using Comsol Multiphysics Fig. 7 shows the local magnetic field distribution outside the NPs and NRs of equivalent material volume at an applied magnetic field of 3 Tesla (the magnetic field distribution profile for NRs of length 60 and 70 nm are shown in Fig. S8, ESI). The simulation results show a significant stronger local field inhomogeneity created by the NRs than the NPs. Moreover, from the surface and further away; the field intensity decreases slowly for NRs than the NPs (Fig. 7), which could be due to an anisotropic shape of the NRs. In general the magnetic field induced outside a magnetized sphere varies with ($1/r^3$), while in case of a cylinder it varies with ($1/r^2$), where 'r' is the distance away from the surface of the spherical/cylindrical rod object.[49] Thus, the rod shape morphology and higher outer sphere diameter of the NRs renders a strong local magnetic field over a larger volume as compared to NPs, although it possesses lower magnetic moment. As a result, a larger number of water

protons experience strong magnetic field over a large volume and rapidly de-phase, consequently higher R_2 value is realized for NRs than of equivalent material volume NPs. While for spherical NPs, due to small volume of magnetic field variations, the water proton slowly diffuse around the nanoparticles and hence slowly de-phase, consequently smaller R_2 value is observed. A detail of the water proton R_2 relaxation due to NPs and NRs is shown as Scheme 2. Further, with an increase of NRs length, the induced local magnetic field strength outside the NRs also increases (Fig S8, ESI) (this enhancement of local magnetic field strength is due to the increase of both the M_S value and the surface area). As a result, with an increase of NRs length from 30 to 70 nm, the R_2 relaxivity value increases linearly from 312 to 608 $s^{-1}mM^{-1}$ (Fig 8a). A similar increasing trend in R_2 relaxivity values is also observed for nanoparticles (Fig 8b). It is of interest to note that, the highest R_2 value 608 $s^{-1}mM^{-1}$ observed for NRs of length 70 nm is nearly six times higher than the value reported for the commercial contrast agent (Ferumoxytol and 85 $s^{-1}mM^{-1}$).[23, 50] In general the rod shaped morphology offers longer blood circulation times and stronger interaction with tumors in comparison to spherical nanoparticles of equivalent hydrodynamic diameter.[31] Hence, we believe that nanorods with superior T_2 weighted contrast properties can improve the clinical diagnosis sensitivity to a great extent.

4. Conclusions

In summary, we have successfully demonstrated a facile amine mediated reduction process for the synthesis of Fe_3O_4 NRs of length 30 – 70 nm and diameter 4 – 12 nm. As compared to conventional spherical nanoparticles, Fe_3O_4 NRs of similar material volume provide a superior T_2 contrast effect with 1.5 – 2 times higher R_2 value. The enhanced MRI contrast properties of nanorods is attributed to higher surface area and anisotropic morphology, which induces a stronger magnetic field perturbation over a larger volume more effectively for the outer sphere protons. With the increases of the length of Fe_3O_4 NRs, R_2 value increases sharply from 312 - 608 $s^{-1}mM^{-1}$. This increasing trend of R_2 values with the length of

nanorods is due to enhancement of magnetization value as well as outer sphere surface area. With a given biocompatibility and poor cytotoxicity, these iron oxide rod shaped structures appear to be a promising contrast agent for MRI applications and in future we would like to further investigate *in vivo* cancer diagnostic studies with such anisotropic functionalized structures.

Acknowledgement: We gratefully acknowledge the Industrial Research and Consultancy Center (IRCC), IIT Bombay and Council of Scientific and Industrial Research (CSIR), New Delhi, Nanomission of the Department of Science and Technology (DST), and the nanotechnology division of Department of Electronics and Information Technology (DEITY) the Government of India for the financial support of this work. We are thankful to Dr Karthik Ganesan, SRL Diagnostics Pvt Ltd, Lower Parel, Mumbai for providing MRI instrument facilities. M. Aslam would also like to acknowledge a financial support from Prof. Vinayak P. Dravid, Materials Science and Engineering Department, Northwestern University, Evanston, IL-60201.

References

1. J. Cheon and J.-H. Lee, *Acc. Chem. Res.*, 2008, **41**, 1630-1640.
2. Y.-w. Jun, J.-w. Seo and J. Cheon, *Acc. Chem. Res.*, 2008, **41**, 179-189.
3. J.-H. Lee, Y.-M. Huh, Y.-w. Jun, J.-w. Seo, J.-t. Jang, H.-T. Song, S. Kim, E.-J. Cho, H.-G. Yoon, J.-S. Suh and J. Cheon, *Nat Med*, 2007, **13**, 95-99.
4. N. Lee and T. Hyeon, *Chem. Soc. Rev.*, 2012, **41**, 2575-2589.
5. J. R. McCarthy and R. Weissleder, *Adv. Drug Delivery Rev.*, 2008, **60**, 1241-1251.
6. E. Terreno, D. D. Castelli, A. Viale and S. Aime, *Chem. Rev.*, 2010, **110**, 3019-3042.
7. D. Yoo, J.-H. Lee, T.-H. Shin and J. Cheon, *Acc. Chem. Res.*, 2011, **44**, 863-874.
8. A.-H. Lu, E. L. Salabas and F. Schüth, *Angew. Chem., Int. Ed.*, 2007, **46**, 1222-1244.
9. J. Gao, H. Gu and B. Xu, *Acc. Chem. Res.*, 2009, **42**, 1097-1107.
10. J.-P. Fortin, C. Wilhelm, J. Servais, C. Ménager, J.-C. Bacri and F. Gazeau, *J. Am. Chem. Soc.*, 2007, **129**, 2628-2635.
11. J.-H. Lee, J.-t. Jang, J.-s. Choi, S. H. Moon, S.-h. Noh, J.-w. Kim, J.-G. Kim, I.-S. Kim, K. I. Park and J. Cheon, *Nat Nano*, 2011, **6**, 418-422.
12. J. S. Weinstein, C. G. Varallyay, E. Dosa, S. Gahramanov, B. Hamilton, W. D. Rooney, L. L. Muldoon and E. A. Neuwelt, *J Cereb Blood Flow Metab.*, 2009, **30**, 15-35.
13. H. B. Na, I. C. Song and T. Hyeon, *Adv. Mater.*, 2009, **21**, 2133-2148.
14. N. Lee, H. Kim, S. H. Choi, M. Park, D. Kim, H.-C. Kim, Y. Choi, S. Lin, B. H. Kim, H. S. Jung, H. Kim, K. S. Park, W. K. Moon and T. Hyeon, *Proc. Natl Acad. Sci.*, 2011, **108**, 2662-2667.
15. J.-t. Jang, H. Nah, J.-H. Lee, S. H. Moon, M. G. Kim and J. Cheon, *Angew. Chem., Int. Ed.*, 2009, **48**, 1234-1238.

16. Z. Li, P. W. Yi, Q. Sun, H. Lei, H. Li Zhao, Z. H. Zhu, S. C. Smith, M. B. Lan and G. Q. Lu, *Adv. Funct. Mater.*, 2012, **22**, 2387-2393.
17. Y. Wang, Y. W. Ng, Y. Chen, B. Shuter, J. Yi, J. Ding, S. c. Wang and S. S. Feng, *Adv. Funct. Mater.*, 2008, **18**, 308-318.
18. Y.-w. Jun, Y.-M. Huh, J.-s. Choi, J.-H. Lee, H.-T. Song, S. Kim, S. Kim, S. Yoon, K.-S. Kim and J.-S. Shin, *J Am Chem Soc.*, 2005, **127**, 5732-5733.
19. R. S. M. Rikken, R. J. M. Nolte, J. C. Maan, J. C. M. van Hest, D. A. Wilson and P. C. M. Christianen, *Soft Matter*, 2014, **10**, 1295-1308.
20. I. Milosevic, H. Jouni, C. David, F. Warmont, D. Bonnin and L. Motte, *J. Phys. Chem. C*, 2011, **115**, 18999-19004.
21. J. Wan, X. Chen, Z. Wang, X. Yang and Y. Qian, *J. Cryst. Growth*, 2005, **276**, 571-576.
22. H. M. Joshi, Y. P. Lin, M. Aslam, P. V. Prasad, E. A. Schultz-Sikma, R. Edelman, T. Meade and V. P. Dravid, *J. Phys. Chem. C*, 2009, **113**, 17761-17767.
23. K. C. Barick, M. Aslam, Y.-P. Lin, D. Bahadur, P. V. Prasad and V. P. Dravid, *J. Mater. Chem.*, 2009, **19**, 7023-7029.
24. M. Aslam, E. A. Schultz, T. Sun, T. Meade and V. P. Dravid, *Cryst. Growth Des.*, 2007, **7**, 471-475.
25. K. C. Barick, S. Singh, D. Bahadur, M. A. Lawande, D. P. Patkar and P. A. Hassan, *J. Colloid Interface Sci.*, 2014, **418**, 120-125.
26. M. K. Jaiswal, M. De, S. S. Chou, S. Vasavada, R. Bleher, P. V. Prasad, D. Bahadur and V. P. Dravid, *ACS Appl. Mater. Interfaces*, 2014, **6**, 6237-6247.
27. Z. Zhao, Z. Zhou, J. Bao, Z. Wang, J. Hu, X. Chi, K. Ni, R. Wang, X. Chen, Z. Chen and J. Gao, *Nat Commun*, 2013, **4,** 2266.
28. K. Kattel, J. Y. Park, W. Xu, H. G. Kim, E. J. Lee, B. A. Bony, W. C. Heo, S. Jin, J. S. Baeck, Y. Chang, T. J. Kim, J. E. Bae, K. S. Chae and G. H. Lee, *Biomaterials*, 2012, **33**, 3254-3261.
29. S. Huang, J. Liu, D. Liu and Q. Yuan, *New J. Chem.*, 2012, **36**, 1335-1338.
30. M.-L. Chen, L.-M. Shen, S. Chen, H. Wang, X.-W. Chen and J.-H. Wang, *J. Mater. Chem. B*, 2013, **1**, 2582-2589.
31. B. Sitharaman, *Nanobiomaterials handbook*, CRC Press, 2011.
32. J. Mohapatra, A. Mitra, D. Bahadur and M. Aslam, *CrystEngComm*, 2013, **15**, 524-532.
33. A. Mitra, J. Mohapatra, S. S. Meena, C. V. Tomy and M. Aslam, *J. Phys. Chem. C,*, 2014, **118**, 19356-19362.
34. A. P. Grosvenor, B. A. Kobe, M. C. Biesinger and N. S. McIntyre, *Surf. Interface Anal.*, 2004, **36**, 1564-1574.
35. T. J. Daou, G. Pourroy, S. Bégin-Colin, J. M. Grenèche, C. Ulhaq-Bouillet, P. Legaré, P. Bernhardt, C. Leuvrey and G. Rogez, *Chem. Mater.*, 2006, **18**, 4399-4404.
36. L.-Y. Chen, Y.-T. Yin, C.-H. Chen and J.-W. Chiou, *J. Phys. Chem. C*, 2011, **115**, 20913-20919.
37. J.-M. Moon and A. Wei, *J. Phys. Chem. B*, 2005, **109**, 23336-23341.
38. S. Mourdikoudis and L. M. Liz-Marzán, *Chem. Mater.*, 2013, **25**, 1465-1476.
39. E. Murad and J. L. Bishop, *Am. Mineral.*, 2000, **85**, 716-721.
40. M. Chen, Y.-G. Feng, X. Wang, T.-C. Li, J.-Y. Zhang and D.-J. Qian, *Langmuir*, 2007, **23**, 5296-5304.
41. J. K. Armstrong, R. B. Wenby, H. J. Meiselman and T. C. Fisher, *Biophys. J.*, 2004, **87**, 4259-4270.
42. P. K. Kandel, L. P. Fernando, P. C. Ackroyd and K. A. Christensen, *Nanoscale*, 2011, **3**, 1037-1045.
43. T. Xia, M. Kovochich, M. Liong, H. Meng, S. Kabehie, S. George, J. I. Zink and A. E. Nel, *ACS Nano*, 2009, **3**, 3273-3286.
44. G. Joaquín and S. Gloria, *J. Phys.: Condens. Matter*, 2004, **16**, R145.
45. W. Friedrich, *J. Phys.: Condens. Matter*, 2002, **14**, R285.
46. J. Mohapatra, A. Mitra, D. Bahadur and M. Aslam, *J. Alloys Compd.*, 2015, **628**, 416-423.
47. J. Wan, Y. Yao and G. Tang, *Appl. Phys. A*, 2007, **89**, 529-532.
48. H. Sun, B. Chen, X. Jiao, Z. Jiang, Z. Qin and D. Chen, *J. Phys. Chem. C*, 2012, **116**, 5476-5481.

49. J. F. Schenck, *Med. Phys.*, 1996, **23**, 815-850.
50. S. Xuan, Y.-X. J. Wang, J. C. Yu and K. Cham-Fai Leung, *Chem. Mater.*, 2009, **21**, 5079-5087.

Figures

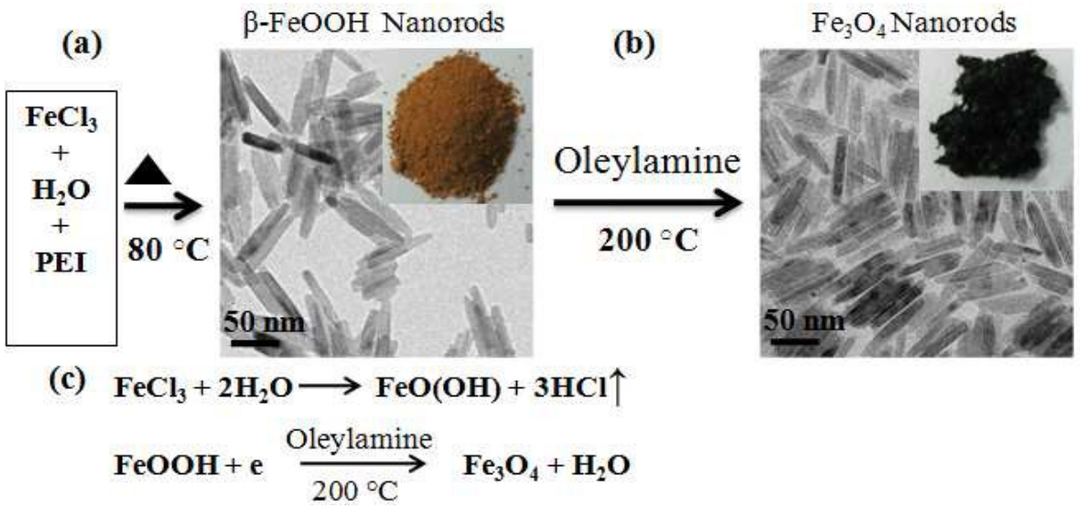

Scheme 1: Schematic representation of the two step synthesis route for Fe_3O_4 NRs. (a) Hydrolysis of $FeCl_3$ (β-FeOOH, orange colored powder), the corresponding TEM images of the sample confirms that rod shaped β-FeOOH of uniform size were formed with a mean length of 70 nm. (b) FeOOH NRs was reduced to Fe_3O_4 phase by using oleylamine as a multifunctional agent (solvent, reducing and capping agent) at 200 °C, shape and size of the rods are retained (TEM image). (c) Possible reaction mechanism for the preparation of Fe_3O_4 NRs from FeOOH NRs.

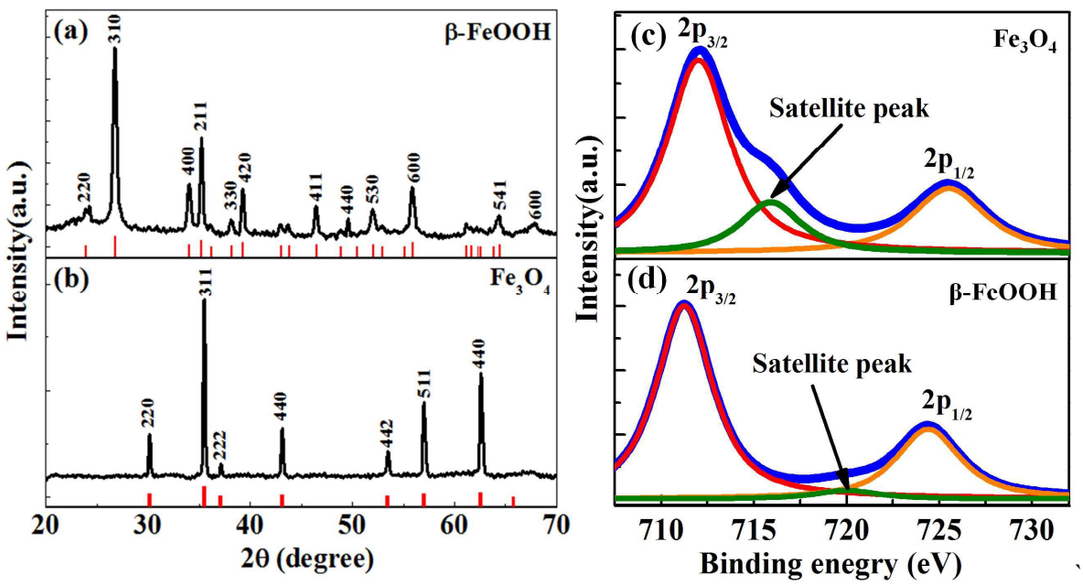

Fig. 1: XRD patterns of (a) as-synthesized β-FeOOH samples of length 70 nm and (b) Fe_3O_4 NRs produced after reduction of β-FeOOH in oleylamine. The XRD patterns of β-FeOOH and Fe_3O_4 are labeled with respect to standard ICDD cards (marked as red). XPS spectra of (c) Fe_3O_4 and (d) β-FeOOH NRs of length 70 nm. After the phase change to Fe_3O_4, the characteristic satellite in the octahedral Fe^{3+} spectrum (β-FeOOH NRs) shifts to 716 eV which indicates the presence of Fe^{2+} in octahedral site of the magnetite phase.[35]

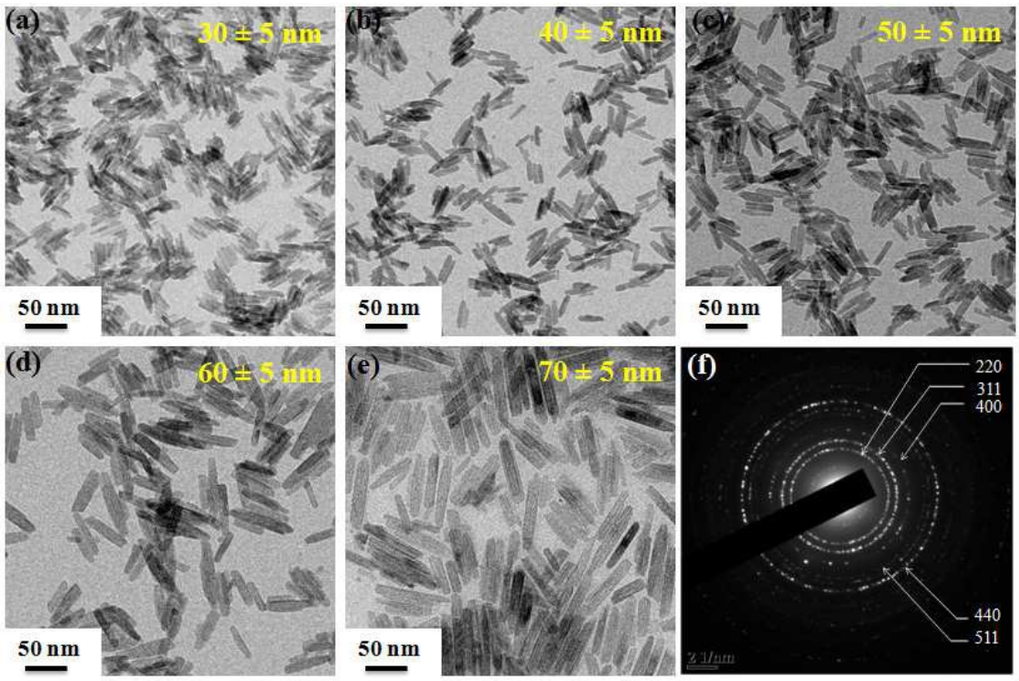

Fig. 2: TEM micrographs of different length Fe_3O_4 NRs: (a) 30 nm, (b) 40 nm, (c) 50 nm, (d) 60 nm and (e) 70 nm. (f) SAED pattern of 70 nm Fe_3O_4 NRs. The SAED pattern shows a set of rings identified as reflection from five crystal planes (220), (311), (400), (511) and (440) of Fe_3O_4.

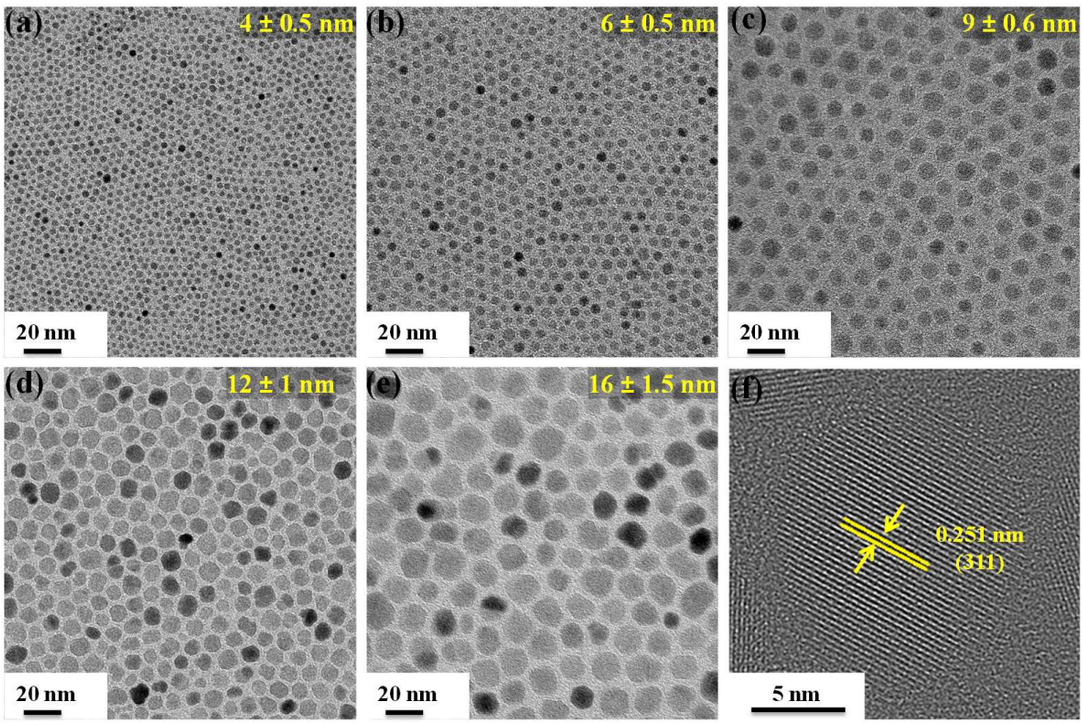

Fig. 3: TEM micrographs of Fe_3O_4 nanoparticles produced through thermolysis of $FeCl_2$ and oleylamine at 200 °C with Fe-amine mole ratio. (a) 1:7 (4 nm), (b) 1:5 (6 nm), (c) 1:3 (9 nm). (d) 12 nm and (e) 16 nm Fe_3O_4 nanoparticles are obtained from seed-mediated growth using 150 mg and 100 mg of 6 nm nanoparticles as initial precursor respectively. (f) HRTEM image of crystalline 12 nm sized Fe_3O_4 nanoparticle.

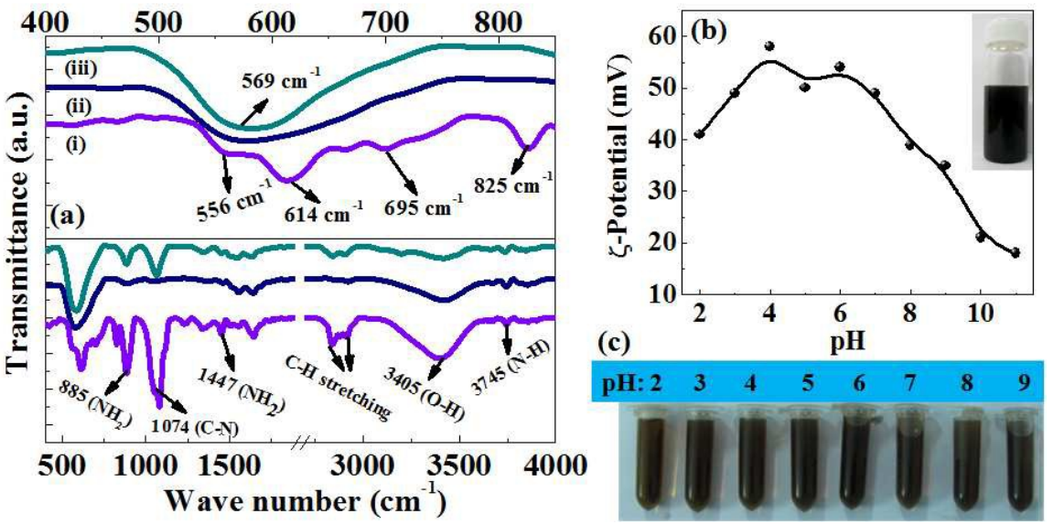

Fig. 4: (a) Comparative analysis of FTIR spectra of Fe-O vibrations (upper half) and surface functional groups (lower half) of: (i) as prepared PEI coated FeOOH, (ii) oleylamine functionalized Fe_3O_4 and (iii) surface modified Fe_3O_4 NRs with PEI. (b) Zeta potential at different pH values of PEI functionalized Fe_3O_4 NRs and inset shows the photo of aqueous suspension of Fe_3O_4 NRs after one month. (c) Digital photograph shows the colloidal stability of Fe_3O_4 NRs (1mg/ml) at different pH conditions.

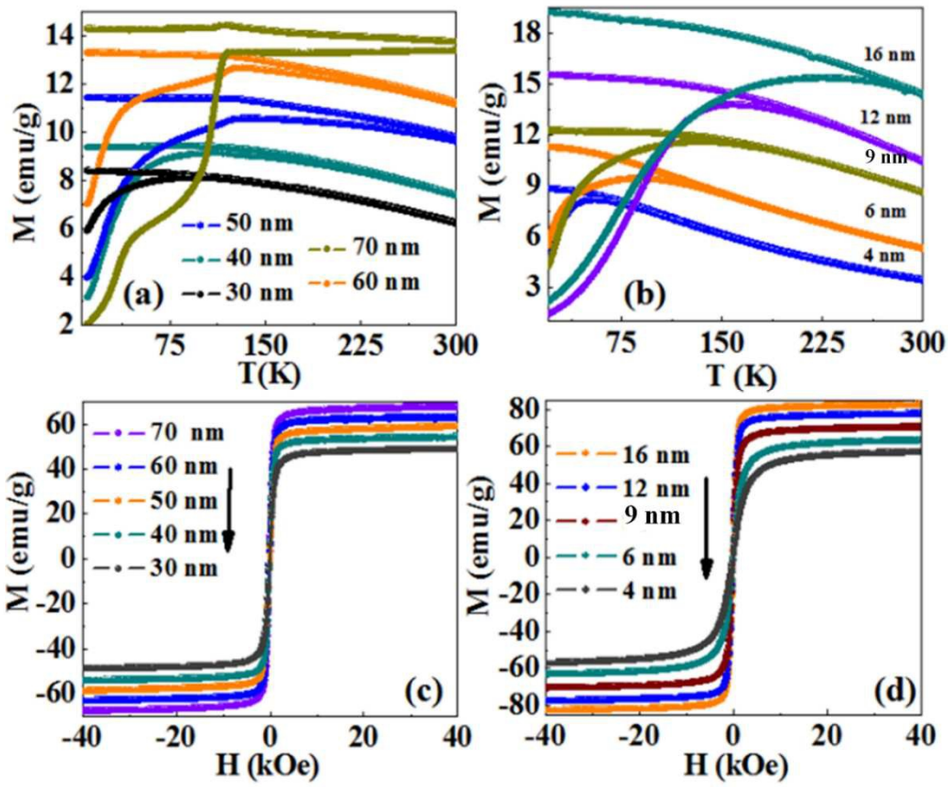

Fig. 5: Field-cooled (FC) and zero-field-cooled (ZFC) magnetization plot of different sizes: (a) nanorods and (b) spherical nanoparticles of Fe_3O_4 at an applied field of 200 Oe. Room temperature field dependent magnetization curves of different sizes of (c) nanorods and (d) spherical nanoparticles of Fe_3O_4.

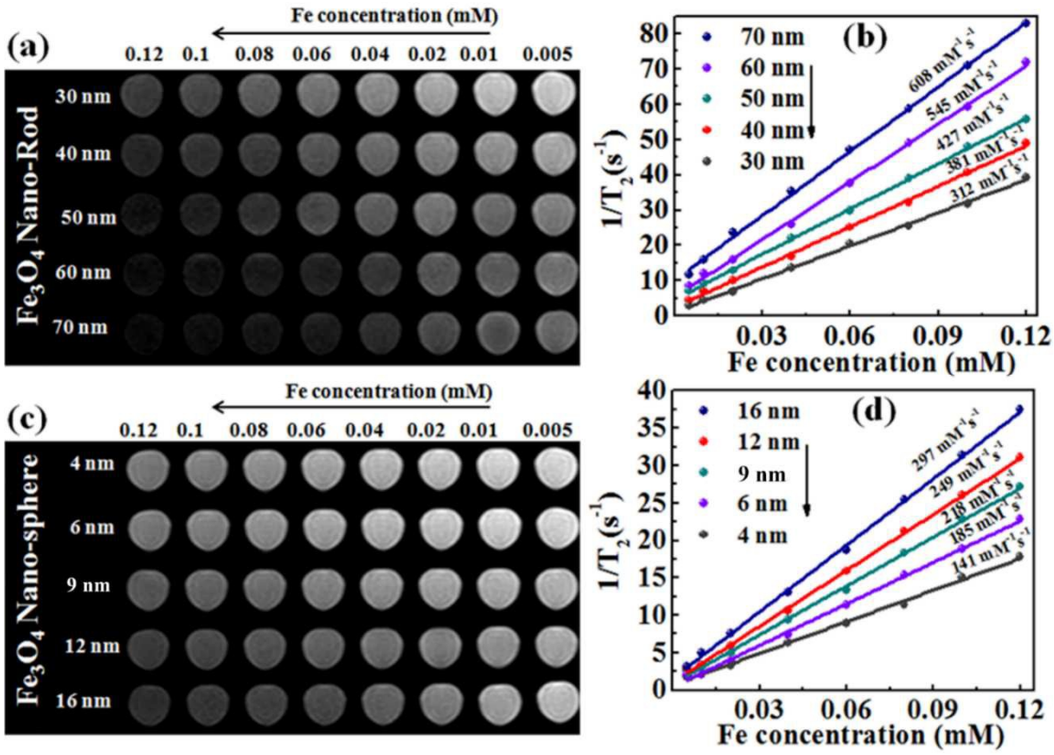

Fig. 6: MR contrast effect of Fe_3O_4 NRs of different length and NPs of different diameter. T_2-weighted MR images of Fe_3O_4 (a) NRs and (c) NPs at various concentrations of iron under an applied magnetic field of 3 T, TR = 3500 ms and TE = 30 ms. Plots of R_2 values of (b) Fe_3O_4 NRs and (d) Fe_3O_4 NPs of different sizes.

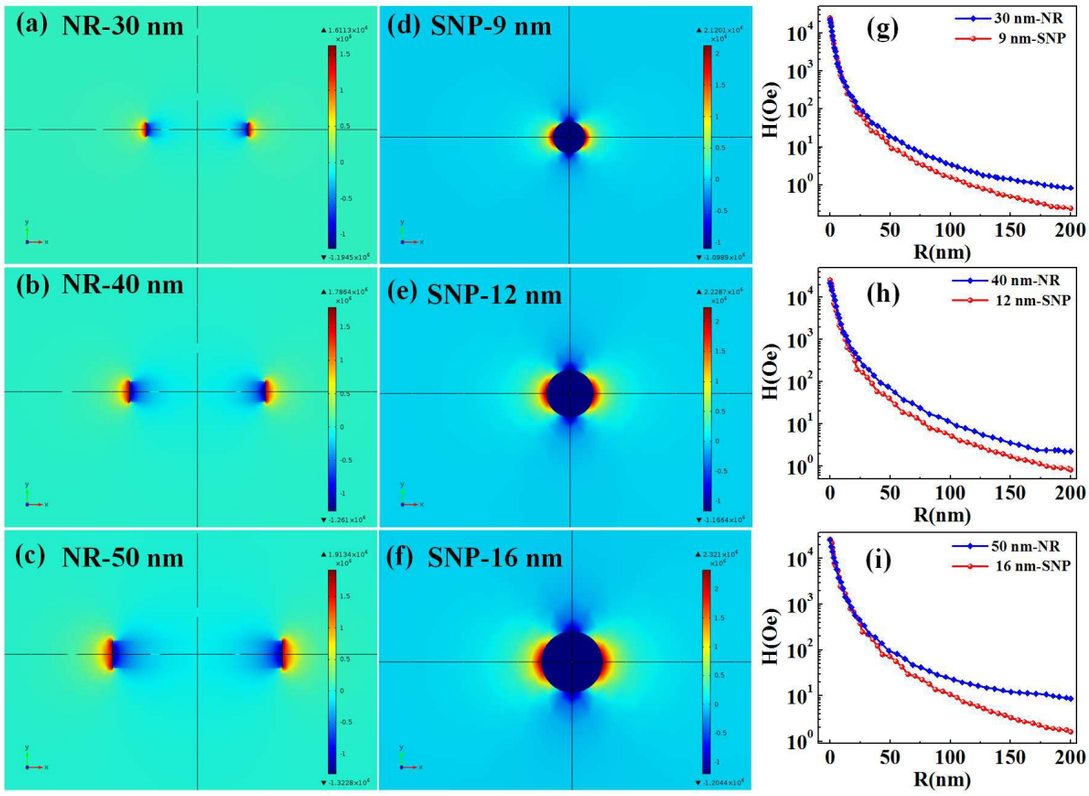

Fig. 7: The local magnetic field generated by the NRs and spherical Fe_3O_4 NPs of equivalent material volume under an applied magnetic field of 3T. Figure (a), (b) and (c) shows the induced magnetic field distribution of 30, 40 and 60 nm iron oxide NRs and Figure (d), (e) and (f) show the field distribution of equivalent material volume NPs of size 9, 12 and 16 nm, respectively. (g), (h) and (i) shows the variation of induced magnetic field with distance 'R' from the surface of NPs and NRs (y-axis is represented at log-scale).

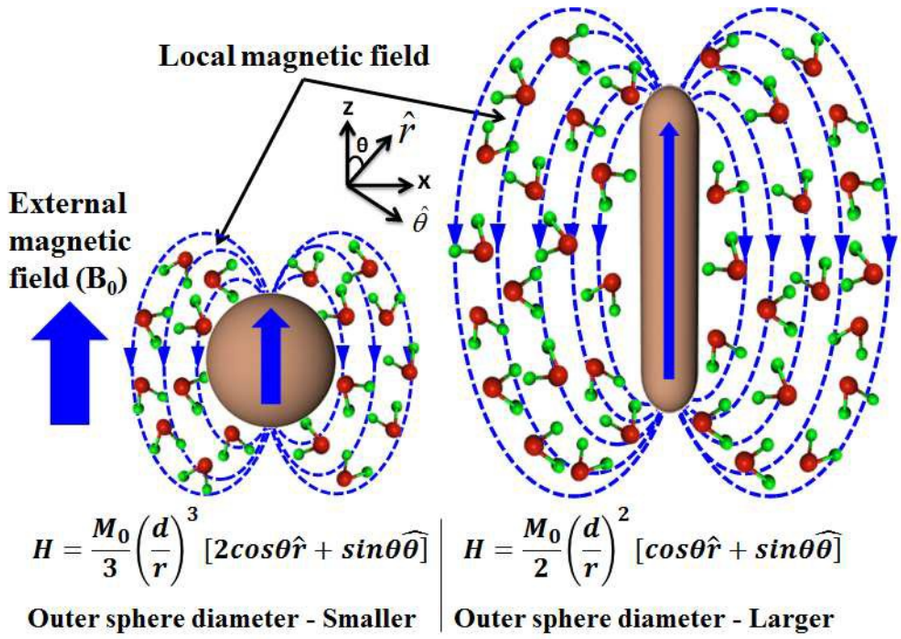

Scheme 2: Schematic representation of quantum mechanical outer sphere model of Fe_3O_4 NPs and NRs of same material volume. H is the induced local magnetic field outside NRs and NPs, where d is the effective diameter, r is the distance between the proton spin and the nanostructure being considered and θ is the inclination angle of the vector joining the proton spin to the nanostructure. In comparison to NPs, the local magnetic field of NRs decreases slowly and hence the strong magnetic field over a larger magnetic volume results in higher R_2 relaxivity

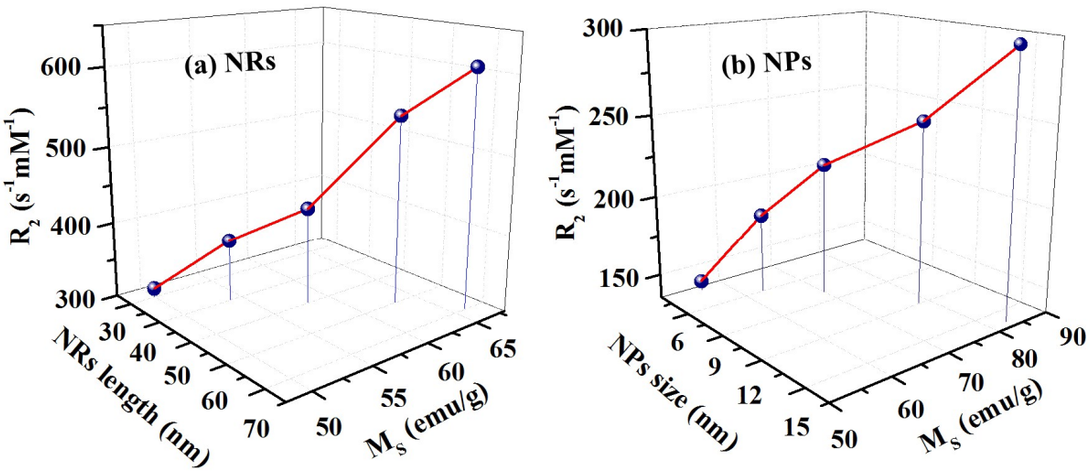

Fig. 8: The variation of R_2 relaxivity value with: (a) the length and M_S value of nanorods and (b) the diameter and M_S value of nanoparticles. With an increase of nanorods size, the R_2 relaxivity values increase linearly from 312-608 $s^{-1}mM^{-1}$. This linear trend is due to an enhancement of M_S value as well as the surface area.